THE EFFECT OF HOLLOW GOLD NANOPARTICLES ON STEM CELL MIGRATION. POTENTIAL APPLICATION IN TISSUE REGENERATION

M. Mar Encabo-Berzosa[†,□], *Maria Sancho-Albero*[†,□], *Alejandra Crespo*[⊥], *Vanesa Andreu*[†,□], *Victor Sebastian*[†,□], *Silvia Irusta*[†,□], *Manuel Arruebo*[†,□,*], *Pilar Martín Duque*[⊥,¬], *Jesus Santamaria*[†,□]

†Department of Chemical Engineering. Aragon Institute of Nanoscience (INA), University of Zaragoza, Campus Río Ebro-Edificio I+D, C/ Poeta Mariano Esquillor S/N, 50018-Zaragoza, Spain.

□Networking Research Center on Bioengineering, Biomaterials and Nanomedicine, CIBER-BBN, 28029-Madrid, Spain.

⊥Universidad Francisco de Vitoria, Facultad de Ciencias Biosanitarias, Carretera Pozuelo a Majadahonda, Km 1.800, 28223 Pozuelo de Alarcón, Madrid, Spain

¬Fundación Araid, Zaragoza, Spain

Introduction

Every year trauma together with bone, joints and cartilage-associated diseases usually involve structural damage, resulting in a severe pain and disability for millions of people worldwide[1]. In regenerative medicine, cellular, tissue and organ-based approaches are developed to restore biological functions that have been lost[2],[3]. Therefore, tissue repair and regenerative medicine have attracted the interest of the scientific community, providing promising results in preclinical models and clinical pilot studies.

Different cells such as mesenchymal stem cells (MSCs) are crucial players in the processes of tissue regeneration. MSCs are progenitor cells that can be differentiated into many cell types and also have the ability to migrate towards damaged tissues[4] (i.e., wounds, tumor sites, inflamed tissues) to help in their repair. Promising results using these cells have already been reported in wound healing, for example in repairing corneal damage[5] or spinal cord injury[6]. Skeletal disorders present many opportunities for the use of MSCs, and numerous clinical trials have shown encouraging results[7]. These cells present a high potential in regenerative medicine where novel therapeutic strategies could be developed, based on different chemical and biological cues.

Nanotechnological tools have often been leveraged for tissue regeneration because some nanoscale properties make cell interactions and other cellular functions (cell adhesion, proliferation and differentiation) far more efficient than traditional macroscopic materials[8]. The capacity of some nanomaterials to speed up the repair of several tissues (such as bone, cartilage, bladder, nerves and vessels) by improving their intrinsic biological functions has been reported[9]. The quantification of the migration

ability and proliferative capacity of cells on different substrates provide valuable insights for new biomaterials design[10]. Numerous *in vitro* and *in vivo* reports have studied the effect of nanoparticles (characteristics such as sizes[11], shapes[12] and surface coatings[13]) in cell migration, proliferation, differentiation and wound healing. For example, internalization of SiO_2 Nanoparticles (NPs) affect essential physiological functions in the cell including adhesion and migration[14]. In the same way, it has been demonstrated that the human endothelial exposition to carbon nanotubes induces an increase in endothelial monolayer permeability and cell migration[15]. Also the effects of TiO_2, SiO_2 and hydroxyapatite NPs in epithelial cell migration have been evaluated, resulting in an increased cell contractility with significantly impaired wound healing capability[16]. Finally, the use of PLGA micro-NPs to promote bone regeneration has also been analyzed. In this sense, the use of PLGA micro-NPs could be an advance in the design of scaffolds, since it allows the encapsulation of inducing bone regeneration growth factors as BMP2. In addition PLGA is biocompatible and biodegradable, which give it advantages over other materials[17].

Gold nanoparticles (GNPs) have attracted the interest of recent research because of their biomedical potential as drug carriers, gene vectors and therapeutic agents in a wide range of promising applications ranging from cancer and neuropsychiatric disorders to tissue repair and regeneration[18]. Their advantages include the ease of synthesis in a varied range of monodisperse sizes, the fact that they are essentially inert and non-toxic at the doses used and their ability to be readily functionalized with targeting ligands and drugs. Recent studies indicate that these nanoscale materials have a direct influence on MSCs behavior from a cellular to a molecular level. Thus, GNPs functionalized with different coatings induce differential MSC response and, when optimized, could promote MSCs proliferation, contributing to the development of new strategies for tissue regeneration therapies[19].

Here we report the potential impact of GNPs on the migration and proliferation behavior of different cell lines: MSCs, HeLa cells and human dermal fibroblasts. GNPs are easily internalized by MSCs causing an increase in their migration rate, mediated by actin and tubulin expression. On the other hand, the migration capacity of tumoral and epithelial cells was not significantly affected by the presence of the nanoparticles at the same doses. Our results provide some insights on the influence of GNPs on cellular behavior (migration, proliferation, differentiation and ability to colonize scaffolds) and show the potential of these materials for strategic regenerative medicine and tissue repair. Incubation of MSCs with GNPs appears as a useful tool to modulate their migration capacity to achieve a more rapid and effective regenerative therapy.

Methods

1. Synthesis of Hollow Gold Nanoparticles

All the materials employed in the HGNs synthesis were provided by Sigma Aldrich and used as received: cobalt (II) chloride hexahydrate, sodium citrate tribasic dihydrate, poly

(vinylpyrrolidone) (PVP) Mw=55000 Da, gold (III) chloride hydrate (50% purity), sodium borohydride, and poly (ethylene glycol)-ether thiol (PEG 1000 Da MW).

HGNs synthesis was carried out following the procedure used in previous works[20]. Briefly, in a two-necked round-bottom flask 400 mL of distilled water, 400 µL of 0.4 M of cobalt chloride hexahydrate ($CoCl_2 \cdot 6H_2O$) and 1.6 mL of 0.1 M sodium citrate trihydrate ($Na_3C_6H_5O_7 \cdot 3H_2O$) were mixed without magnetic stirring under an inert Ar atmosphere to avoid a premature Co oxidation. After 40 minutes, 2 mL of a 1 wt. % solution of poly (vinylpyrrolidone) (PVP) with an average Mw of 55000 Da and 400 µL of 1.0 M sodium borohydride ($NaBH_4$) were added. The color change from pale pink to brown was indicative of the cobalt nanoparticle formation. Subsequently, 120 mL of distilled water and 180 µL of 0.1M chloroauric acid trihydrate ($HAuCl_4 \cdot 3H_2O$) were mixed with 360 mL of the previous cobalt-based dispersion used as sacrificial template to promote the formation of $CoCl_2$, CoO and the and the galvanic reduction of Au^{3+} obtaining hollow Au-based shells.

The resulting HGNs were functionalized with PEG (steric polymer) to obtain PEG-HGNs using an excess of monofunctional poly (ethylene glycol)-ether thiol (PEG 1000 Da MW), taking advantage of the strong chemical bond between Au and S. A solution of HGNs was put in contact with a dilution of PEG during one hour under magnetic stirring. Any excess of unbound PEG was removed by dialysis.

The concentration of the final dispersion was adjusted by centrifugation at 10000 rpm for 10 minutes.

2. Nanoparticle characterization

Size, shape and surface chemistry are all important properties for determining the specific properties and characteristics of NPs. The morphology and size distribution of HGNs and PEG-HGNs were characterized by transmission electron microscopy (T20-FEI Tecnai thermoionic transmission electron microscope) operated at 200 kV with a LaB6 electron source fitted with a "SuperTwin®" objective lens allowing a point-to-point resolution of 2.4 Å. From the TEM images, an average particle diameter was obtained for HGNs and PEG-HGNs with ImageJ software (NIH-RSB). Using UV-VIS spectroscopy (Jasco V670) the characteristic plasmon at a particular wavelength of HGNs and PEG-HGNs was evaluated, and related with their size and shape.

Thermogravimetric analysis (TGA; Mettler Toledo TGA/STDA 851e) was carried out in a temperature range between 30 and 850 ºC with a heating rate of 20 ºC/min to assess the PEG/Au weight ratio in the NPs. In order to analyze the stability and the surface charge of the particles, zeta potential assay at pH=7 was also performed (Brookhaven 90 plus and ZetaPALS software). The NPs were resuspended and measured in a 1mM KCl solution at a pH=7. Finally, X-ray photoelectron spectroscopy (XPS) was used to determine the elemental composition and the surface grafting of PEG-HGNs. It was performed with an Axis Supra (Kratos Tech.). The spectra were collected by using a monochromatized AlKa source (1486.6 e.V) run at 15 kV and 15 mA. For the individual peak regions, a pass energy

of 20 eV. was used. Analyses of the peaks were performed with the CasaXPS software, using a weighted sum of Lorentzian and Gaussian component curves after background subtraction.

3. Cell culture conditions

Murine MSCs, human dermal fibroblasts and HeLa cells were obtained from Lonza and Cancer Research-UK cell services. MSCs were cultured in Dulbecco's modified Eagle's F-12 medium (DMEM F-12, GIBCO) with 10% fetal bovine serum (FBS, GIBCO), 1% penicillin/streptomycin and 1% amphotericin and maintained at 37°C in a 5% CO_2-humidified atmosphere under hypoxic conditions (3% O_2). For culturing fibroblasts and HeLa cells Dulbecco's modified Eagle's medium (DMEM, GIBCO) with 10% fetal bovine serum (FBS, GIBCO), 1% penicillin/streptomycin and 1% amphotericin were used under normoxic conditions.

4. Nanoparticles cellular uptake

Confocal microscopy characterization (Spectral Confocal Microscope Leica TCA SP2) was carried out to evaluate the cellular uptake and trafficking of PEG-HGNs in the different cell types. Cells were seeded at a density of 2 x 10^4 cells onto 20 mm cover slips (in a 24-well plate) and allowed to grow for 24 h. The PEG-HGNs (50 μg mL^{-1}) were incubated with the different cellular types during one day. After that, cells were fixed with para-formaldehyde 4% and marked with phalloidin-Alexa488 (Invitrogen) to label the cytoplasmic actin and with Draq-5 to label the nuclei. PEG-HGNs-based agglomerates were directly observed by reflection of the incident light in the confocal microscope at 488/490 nm excitation/emission wavelengths. Z-stack orthogonal projections were carried out in order to analyze the presence of PEG-HGNs inside the cytosol.

5. Scratch assay

To study the role of PEG-HGNs in cell migration scratch assays were carried out. First, 2 x 10^5 cells (MSCs, fibroblasts and HeLa) were seeded onto 6 multi-well culture plates and 24 h later 50 μg mL^{-1} of PEG-HGNs was added to the cells. The control wells were maintained without nanoparticles. When a homogenous monolayer of cells was achieved, a 1 mm wide straight line indentation was made with a 1000 μL pipette tip simulating a wound. Cells were washed twice with PBS and visualized in an inverted optical microscope (Olympus IX81) at 0h, 4h and 24 h after scratching. The data were statistically analyzed taking five independent measurements in three different zones of the wound.

6. Immunoassay and confocal microscopy

Tubulin and actin expression in MSCs, fibroblasts and HeLa cells was evaluated by confocal microscopy. First, cells were seeded onto 20 mm sterile cover slips (in a 24-well plate) at a density of 2 x 10^4 cells per well and allowed to grow during 24 h. After that time, PEG-HGNs were added to the cells at a concentration of 50 μg mL^{-1} keeping the incubation for

24 h. Subsequently, cells were washed three times with PBS and fixed with para-formaldehyde 4% during 20 minutes.

The immunoassay was done as follows: cells were permeabilized with 0,1% PBS-BSA saponin. Afterward, they were incubated for 1 h at room temperature in a wet chamber with the specific antibodies. For actin labeling, a phaloidin-Alexa488 (Invitrogen) was used. In the case of tubulin, not only a primary antibody against α-tubulin (Invitrogen) was employed, but also an immunofluorescence-conjugated secondary antibody (Zymed Laboratories) was needed. In that case, a pre-blocking with 5% PBS-BSA was performed. Next, the cover-slips were mounted in the holders with mowiol containing Draq5 and visualized by confocal laser scanning microscopy (Spectral Confocal Microscope Leica TCA SP2). Finally, the fluorescence intensity, corresponding with the protein expression level, was measured using Confocal Uniovi ImageJ software (NIH-RSB).

7. Cell cycle evaluation

To study the effect of HGNs on the proliferation rate of the different cell types, the distribution of cell-cycle phases after NPs treatment was assessed by flow cytometry. First of all, cells were seeded onto 6-well plates at a density of 2,5 x 10^5 cells per well. After 24 h of maintenance, PEG-HGNs (50 μg mL^{-1}) were added into the treated wells. One day later, cells were trypsinized and washed twice with PBS (1200 rpm, 5 min). Finally, cells were collected in PBS and fixed with 70% ice-cold ethanol (1 x 10^6 cells per mL) and maintained at 4 ºC in these solution almost for 24 h. DNA staining was performed by adding RNase A and propidium iodide to the cell solution. Finally, samples were analyzed in a FACSARRAY BD equipment with the MODIFIT 3.0 Verity software. Control samples (not treated cells) were also run to know the standard distribution of cell cycle in the cell lines assayed.

8. Mesenchymal stem cells differentiation

The adipogenic and osteogenic differentiation capacity of MSCs was evaluated in presence or absence of PEG-HGNs. Briefly, cells were allowed to grow until the appropriate confluence and the different induction medium was added. On the one hand, induction adipogenic medium (Stem Cells Technologies) was changed every 2-3 days. Cells were maintained in that medium during 14 days. The final concentration of PEG-HGNs in the culture was 50 μg mL^{-1}. At the end of the experiment cells were recovered for RNA extraction. On the other hand, osteogenic induction medium (R&D systems supplements) was also changed every 2-3 days keeping the same final PEG-HGNs concentration (50 μg mL^{-1}). In that case cells were cultured with the induction medium for 21 days. After that time total RNA was purified from the cells.

9. Real time PCR

The total RNA was isolated from mesenchymal stem cells treated or not with PEG-HGNs during the osteogenic or adipogenic differentiation induction experiments. Reverse transcription was performed using the PrimeScript™ Reverse Transcriptase kit (Takara). The relative mRNA expression of the osteogenic differentiation marker genes was normalized

to the GADPH gene and expressed as a fold change relative to the undifferentiated control. Calculations of quantification relative to gene expression were carried out using the $2^{\Delta\Delta Ct}$ method[21]. The $2^{\Delta\Delta Ct}$ method expresses the proportion obtained from the relationship between the Ct values of the sample of interest and the Ct values of the control sample as expressed in the following equation:

Induction, relative quantity (RQ): $2^{[\Delta Ct\ (sample) - \Delta Ct\ (calibrator)]}$

$\Delta Ct\ (sample) = Ct\ (H)_m - Ct\ (P)_m$

$\Delta Ct\ (calibrator) = Ct\ (H)_c - Ct\ (P)_c$

The polymerase chain reaction (PCR) conditions were: an initial step at 95°C for 30 seconds, 40 denaturation cycles of 95°C for 5 seconds and annealing at 60°C for 34 seconds. The following table shows the nucleotidic sequence of the studied genes.

GENE	Primer sequence
Osteopontin (OPN)	5'-CTTTCACTCCAATCGTCCCAC-3' 5'-CAGAAACCTGGAAACCTGGAAACTCCTAGAC-3'
Runx2	5'-CGTCCACTGTCACTTTAATAGCTC-3' 5'-GTAGCCAGGTTCAACGATCTG-3'
Bmp2	5'-TGCAGATGTGAGAAACTCGTC-3' 5'-CGCAGCTTCCATCACGAA-3'
PPAR-ɤ	5'-CTGGCCTCCCTGATGAATAAAG-3' 5'-AGGCTCCATAAAGTCACCAAAG-3'
CD44	5'-CAGTCACAGACCTACCCAATTC-3' 5'-GTGTGTTCTATACTCGCCCTTC-3'
β-actine	5'-GAGGTATCCTGACCCTGAAGTA-3' 5'-CACACGCAGCTCATTGTAGA-3'
Gadph	5'-GTGGAGTCATACTGGAACATGTAG-3' 5'-AATGGTGAAGGTCGGTGTG-3'

10. Scaffold colonization

In order to probe that MSCs incubated with PEG-HGNs (50 μg mL^{-1}) were able to colonize different scaffolds, they were seed onto fibrin or polycaprolactone (PCL) scaffolds. Fibrin scaffolds were prepared following our previous report[22]. Polycaprolactone scaffolds were prepared by electrospinning using an Yflow 2.2.D-500 electrospinner (Electrospinning Machines/R&D Microencapsulation, Malaga, Spain). In brief PCL pellets were dissolved in DCM/DMF (1:1) and the solution was stirred overnight. The polymer solution was then electrospun using a voltage of 10.25 kV. The flow rate and the spinning distance were fixed to 0.5 mL/h and 19 cm., respectively. The spun fibers were collected on a static plate (covered with aluminum foil) connected to negative voltage power supply, at a voltage of 3.11 kV for 18 hours.

Briefly, 4×10^4 of control cells or cells incubated with PEG-HGNs were seeded in the center of PCL membranes (into MW-24 culture plates). One hour later, 600 μL of culture medium were added to each well. Then, cells were incubated during 24 h more. Next, PCL membranes were fixed with 4% paraformaldehyde during 20 min at room temperature.

After two washing cycles with PBS the membranes were placed on a microscopy slide and cell nuclei were stained with Draq5 diluted in Mowiol. Subsequently, a cover was placed on the membranes for facilitating visualization by confocal microscopy. Samples were observed on a Leica TCA SP2 confocal microscope. In all cases, Z acquisitions of different sample areas were performed in order to visualize different planes of the membrane.
In parallel, 3,75 x 10^4 control or pre-incubated with NPs (50 µg mL^{-1}) MSCs were seeded onto fibrin gels. In this case the MSCs employed were able to express the GFP protein, which facilitated their visualization by fluorescence microscopy. The GFP positive cells were kindly provided by Rebeca González. In this experiment, different planes of the gels were acquired at different times in a multidimensional microscope with real time control Leica AF6000 LX, which allowed visualizing the *in vivo* colonization of the gel.

11. Statistical analysis

All the data was expressed as the mean ± standard deviation and all the experiments were performed in triplicate. The statistical analysis of the data with normal distribution was performed using the Student's t-test and one way analysis of variance using software Stata/SE 12.0. For the data groups with a non-normal distribution, the Wilkonson Rank Sum test and the Kruskal-Wallis test were employed. $p<0,05$ was considered statistically significant.

Results and discussion

Nanoparticle characterization

Figure 1 shows TEM images of the as-prepared nanoparticles. The morphology of the obtained nanoparticles was pseudo-spherical with a thick shell visualized in the TEM images as a dark ring. The functionalization with PEG resulted in an external polymeric shell as a halo of almost 4 nm surrounding the HGNs (Figure 1, top, far right). After pegylation no changes in the morphology or the stability of the nanoparticles were observed. The mean size of HGNs was 38.01 ± 5.4 nm, while of PEG-HGNs was 41.7 ± 4.4 nm. A maximum absorbance peak was observed in the NIR region, precisely at 808 nm, which corresponds with the geometrical shape and size observed in TEM images according to the literature[23]. At pH=7 the surface charge of the HGNs and the PEG-HGNs, measured by DLS, was -12.63 ± 0.66 and -7.51± 1.53, respectively. TGA analysis (Figure 1c) showed that the quantity of PEG in the functionalized nanoparticles was around 30% of the total nanoparticle mass. XPS analysis (Figure 2) revealed that in addition to gold oxygen and carbon were also present on the surface even in HGNs, which was mainly attributed to the presence of PVP on the surfaces in agreement with our TGA results (Figure 1c) where approx. a 20 % of the nanoparticle weigh corresponds to organic matter. The PEG used for the functionalization contained sulfur due to the presence of the thiol group in the molecule. This sulfur was also observed in PEG-HGNs, and can be used to trace the presence of PEG on the particles. Also, the chemical environment of gold and sulfur atoms

can be studied to assess the chemical bonding between PEG and the gold NPs. A peak displacement to higher binding energies was observed in the chemical environment of gold, possibly due to union between gold and sulfur. This suggests that the interaction between PEG and HGNs occurs thank to a gold-sulfur bond. We also observed that almost the 90% of the gold was linked to the sulfur. This is consistent with previously published results[24].

Nanoparticle cytotoxicity and uptake

The AlamarBlue® analysis showed that PEG-HNGs did not decrease cell viability at the studied doses (10, 20, 50, 100 and 200 μg mL^{-1}) in any of the cell types of interest (MSCs, HeLa and fibroblasts). In contrast, a dose-dependent cell viability decrease was observed for the non-pegylated HGNs with a marked cytotoxicity at doses above 100 μg mL^{-1} after 24 h of contact for the three cellular types (Figure 3). The dose of 50 μg mL^{-1} PEG-HGNs was chosen for the next experiments as the limit of sub-cytotoxic dose. These results are in agreement with previous studies demonstrating that nanoparticle cytotoxicity was reduced after pegylation[25].

Nanoparticle uptake is influenced by factors such as the physical properties (e.g. size, surface charge) of the nanomaterial or variations in cell-membrane characteristics[26,27]. Confocal microscopy experiments showed large amounts of PEG-HGNs clearly internalized in MSCs forming aggregates inside vesicles (shown as red-colored agglomerates in Figure 4), probably following the endosomal route. Moreover, these NPs were only distributed in the cytoplasm rather than in the nuclei of MSCs because of their size[28],[29]. Unlike MSCs, a significantly lower accumulation of PEG-HGNs was observed inside fibroblast or HeLa cells. It is important to point out that cells were washed before observation, hence any non-internalized nanoparticle would be washed away and only the internalized ones can be observed.

Nanoparticle influence on cell properties

a) Migration evaluation

A variety of physiological and pathological processes such as embryonic development, blood vessel formation and remodeling, tissue regeneration, immune surveillance and inflammation are strongly dependent on the cell migration mechanism[30]. In order to study the capacity of PEG-HGNs as modifiers of cellular behavior for either stem-cell based strategies, or regenerative medicine, some comparative migration experiments were performed following the scratch assay after incubating the three cell types tested with PEG-HGNs during 24h. The assay revealed that PEG-HGNs only significantly influenced MSCs migration but not the other cell types studied. On MSCs, they caused a clear increase in the migration rate compared to untreated cells ($p < 0.05$) (Figure 5). The untreated cells reached a 65% of wound closure 24 h after the scratch, whereas

cells treated with NPs closed almost 90% of the bare surface. However, migration in HeLa cells and fibroblasts was not clearly affected and their migration capacity was significantly smaller than the migration rate of MSCs at 24 h (Figure 5). These results can be explained at least in part by the fact that PEG-HGNs were readily internalized by MSCs, but not by the other cell types. In addition, the limitation of plate adhesion was ruled out as a possible cause of migration induction, since the effect was only observed in MSCs. To test this, the expression of an adhesion rule protein (vinculin) was studied, without any observed effect on that expression. The expression of proteins involved in cell adhesion and migration such as actin, tubulin and vinculin[31] was studied in cells incubated with PEG-HGNs and control cells. The immunoassay revealed that MSCs incubated with PEG-HGNs showed an increased expression rate of actin and tubulin with respect to control cells, being this expression almost 4 times higher (Figure 6). On the other hand, the vinculin expression was not affected. Here, we propose that the increment observed in the closure's speed was probably due to this enhancement in the actin and tubulin expression. It is important to remark that the expression level of the two structural proteins studied (actin and tubulin) in the different cellular types treated with PEG-HGNs was analyzed by quantifying their fluorescence level using the confocal microscopy and the appropriate software to analyze fluorescence. In order to compare the protein expression levels, all the samples were observed under the same optical conditions as the control. On the contrary, both fibroblast and HeLa cells treated with PEG-HGNs showed a similar tubulin and actin expression compared to the control. Therefore, only those cellular types capable to significantly internalize PEG-HGNs increased their migration rate via an increment in actin and tubulin expression. These results are highly promising because cells involved in regeneration such as MSCs, were able to internalize the NPs studied, while the tumoral cells studied here (HeLa) did not show any increase in their migration capacity. While most of the published results today regarding the effects of nanoparticles in scenarios relevant to regenerative medicine show limitations or inhibition of cell migration and proliferation[14],[32],[33], the results of this work evidence the potential of HGNs as performance enhancers in stem-cell based strategies.

b) Proliferation evaluation by cell cycle analysis

No significant differences were found in the cell cycle phase percentages for MSCs or HeLa cells when treated with PEG-HGNs compared to the control (Figure 7). Consequently, we can conclude that the arrest of cell cycle or the damage in the DNA was not induced by PEG-HGNs at the studied doses in these cellular types. Only in human dermal fibroblast, the G1 phase was markedly diminished while the S phase was increased. The affection of the cell cycle is greatly dependent of cellular and nanomaterial type. Uz et al.[34] have recently described that different GNPs with varying degrees of PEG grafting density may affect the cell cycle in different manners. Also it was reported that titanium nanoparticles might affect the MSCs cell cycle in a negative way by increasing the G1 phase and decreasing the G2 and S phases[33].

c) MSCs differentiation studies

MSCs differentiation is a key step in various tissue regeneration processes, such as bone formation. However, the reports on the influence of GNPs on the differentiation process are scarce and their mechanism of action is still under debate. Some studies have shown that GNPs enhance osteogenic differentiation and decrease adipogenic differentiation[19,35]. Li et al.[36] proposed that different gold nanospheres might provide mechanical signals that increase YAP activity and consequently induce osteogenic gene expression, as Runx2. The same research showed that larger spheres, stars or rods did not affect cell differentiation and 40 nm nanorods even reduced the YAP activity. Zhang et al.[37] described the stimulation of the ERK/MAPK signaling pathway in primary osteoblasts mediated by GNPs. Also Wan-Kyu et al.[11] reported the positive effect of different sizes of GNPs in osteogenic differentiation, as well as Yi et al.[38] who concluded that the mechanism involved in the differentiation promoted by 20 nm GNPs was the p38 MAPK pathway modification.

In our study, real time PCR results showed that Runx2 expression was increased in MSCs incubated with PEG-HGNs and differentiated to osteoblasts, compared to the negative control, to a greater extent compared to differentiated MSCs without NPs (Figure 8). Since it has been described[37,39] that Runx2 is regulated by MAPK pathway, we propose that PEG-HGNs might interact with this protein cascade and therefore acting by a mechanical stimulus.

d) Scaffolds colonization

For an initial assessment of the potential application of the MSCs / PEG-HGNs combination in regenerative medicine, the ability of these cells to colonize different types of scaffolds was studied. As can be seen in Figure 9, both control MSCs and those that had been cultured in the presence of PEG-HGNs were able to colonize the PCL scaffold efficiently 24 h after seeding. Qualitatively, cells pre-incubated with PEG-HGNs colonized the scaffold more homogeneously than control cells, as indicated by the greater number and better distribution of nuclei visible in similar areas of the scaffold.

Colonization studies of fibrin scaffolds were also carried out. In this case the ability of cells incubated or not with NPs to colonize fibrin scaffolds with or without NPs (Figure 9) was analyzed. In all cases an efficient colonization of the different gels was observed. The improvement in cell viability and proliferation mediated by the addition of GNPs to scaffolds has recently been reported. They probed that the attachment of GNPs and hydroxyapatite NPs to scaffolds improved the proliferation and viability of fibroblast. They proposed that the observed proliferation increase may be due to the high surface energy of NPs that could affect protein adsorption. Protein adsorption influences cell response to nanoparticles and may enhance cell proliferation[40]. On the other hand, Baranes et al.[41] observed the beneficial effect of GNPs on the differentiation, proliferation and maturation of cultured neurons on 3D scaffolds. In this case the addition of GNPs provided additional anchor sites that allowed for greater morphogenesis. In accordance with that study, the role of GNPs needs to be more investigated, in order to determine whether the NPs

promote axon elongation and higher expression of neuronal markers due to topographical cues or due to their conductivity.

Here, we demonstrated that MSCs containing PEG-HGNs are able to successfully colonize fibrin and PCL-based scaffolds being the NPs responsible for a faster migration rate compared to the control cells as seen in the scratch assay. In addition, an enhanced osteoblastic differentiation also highlights the potential use of nanoparticle-laden cells in regenerative medicine.

Conclusions

HGNs have been used in different biomedical applications as heat transducers in tumor photothermia treatments. Nevertheless, their use as promoters in regenerative medicine has not been studied in depth. The results here proposed are very promising because PEG-HGNs are able to induce MSCs migration whereas this effect is not observed in tumoral cells. Also the enhancement in osteogenic differentiation could open new horizons for the use of PEG-HGNs in the design of biomaterials as scaffolds for bone regeneration. Although more studies are still necessary, our data provide evidence of the possibility of combining MSCs and HGNs in the development of new materials with possible application in regenerative medicine.

Acknowledgements
Financial support from the EU thanks to the ERC Consolidator Grant (ERC-2013-CoG-614715, NANOHEDONISM) is gratefully acknowledged. CIBER-BBN is an initiative funded by the VI National R&D&i Plan 2008–2011, Iniciativa Ingenio 2010, Consolider Program, CIBER Actions and financed by the Instituto de Salud Carlos III (Spain) with assistance from the European Regional Development Fund.
We are grateful to the Scientific Services of the Aragon Institute of Health Sciences and to the LMA.

[1] T. G. Koch, L. C. Berg, D. H. Betts, *CVJ* **2009**, *50*, 155–165.
[2] B. A. Nasseri, K. Ogawa, J. P. Vacanti, *Surgery* **2001**, *130*, 781–784.
[3] R. Atala, A.Lanza, R., Thomson, J. A., & Nerem, *Principles of Regenerative Medicine*, El Servier, Canada, **2010**.
[4] I. R. Murray, C. C. West, W. R. Hardy, A. W. James, T. S. Park, A. Nguyen, T. Tawonsawatruk, L. Lazzari, C. Soo, B. P??ault, *Cell. Mol. Life Sci.* **2014**, *71*, 1353–1374.
[5] B. Demirayak, N. Yüksel, O. S. Çelik, C. Subas, G. Duruksu, Z. S. Unal, D. Kürs, E. Karaöz, *Exp. Eye Res.* **n.d.**, DOI 10.1016/j.exer.2016.08.011.
[6] F. R. Melo, R. B. Bressan, S. Forner, A. C. Martini, M. Rode, P. B. Delben, G. A. Rae, C. P. Figueiredo, A. G. Trentin, *Cell. Mol. Neurobiol.* **2016**, DOI 10.1007/s10571-016-0414-8.
[7] H. Saeed, M. Ahsan, Z. Saleem, M. Iqtedar, M. Islam, Z. Danish, A. M. Khan, *J. Biomed. Sci.* **2016**, *23*, 41.

[8] O. V Salata, *J. Nanobiotechnology* **2004**, *6*, 1–6.
[9] K.-B. L. Aniruddh Solanki, Jonh D Kim, *Futur. Med.* **2008**, *3*, 567–578.
[10] A. Tremel, A. Cai, N. Tirtaatmadja, B. D. Hughes, G. W. Stevens, K. A. Landman, A. J. O. Connor, *Chem. Eng. Sci.* **2009**, *64*, 247–253.
[11] W.-K. Ko, D. N. Heo, H.-J. Moon, S. J. Lee, M. S. Bae, J. B. Lee, I.-C. Sun, H. B. Jeon, H. K. Park, I. K. Kwon, *J. Colloid Interface Sci.* **2015**, *438*, 68–76.
[12] X. Huang, X. Teng, D. Chen, F. Tang, J. He, *Biomaterials* **n.d.**, *31*, 438–448.
[13] C. Lambertz, S. Pierrat, M. Tarantola, D. Schneider, E. Sunnick, A. Janshoff, C. S??nnichsen, *Beilstein J. Nanotechnol.* **2014**, *5*, 2479–2488.
[14] Y. Zhang, L. Hu, D. Yu, C. Gao, *Biomaterials* **2010**, *31*, 8465–8474.
[15] M. Pacurari, Y. Qian, W. Fu, D. Schwegler-Berry, M. Ding, V. Castranova, N. L. Guo, *J. Toxicol. Environ. Heal. Part A* **2012**, *75*, 112–128.
[16] C. Y. Tay, P. Cai, M. I. Setyawati, W. Fang, L. P. Tan, C. H. L. Hong, X. Chen, D. T. Leong, *Nano Lett.* **2014**, *14*, 83–88.
[17] I. Ortega-Oller, M. Padial-Molina, P. Galindo-Moreno, F. O'Valle, A. B. Jódar-Reyes, J. M. Peula-García, *Biomed Res. Int.* **2015**, 2–18.
[18] S. Song, Y. Hao, X. Yang, P. Patra, J. Chen, *J. Nanosci. Nanotechnol.* **2016**, *16*, 2582–2586.
[19] J. J. Li, N. Kawazoe, G. Chen, *Biomaterials* **2015**, *54*, 226–236.
[20] V. Cebrian, F. Martin-Saavedra, L. Gomez, M. Arruebo, J. Santamaria, N. Vilaboa, *Nanomedicine* **2013**, *9*, 646–656.
[21] K. J. Livak, T. D. Schmittgen, *Methods* **2001**, *25*, 402–408.
[22] F. M. Martin-Saavedra, V. Cebrian, L. Gomez, D. Lopez, M. Arruebo, C. G. Wilson, R. T. Franceschi, R. Voellmy, J. Santamaria, N. Vilaboa, *Biomaterials* **2014**, *35*, 8134–8143.
[23] N. Fairbairn, A. Christofidou, A. G. Kanaras, T. a Newman, O. L. Muskens, *Phys. Chem. Chem. Phys.* **2013**, *15*, 4163–4168.
[24] C. Fernandes, C. Pereira, A. Guedes, S. L. H. Rebelo, C. Freire, *Appl. Catal. A Gen.* **2014**, *486*, 150–158.
[25] B. Díaz, C. Sánchez-Espinel, M. Arruebo, J. Faro, E. de Miguel, S. Magadán, C. Yagüe, R. Fernández-Pacheco, M. R. Ibarra, J. Santamaría, et al., *Small* **2008**, *4*, 2025–34.
[26] A. M. Alkilany, C. J. Murphy, *J. Nanoparticle Res.* **2010**, *12*, 2313–2333.
[27] B. Chithrani, A. Ghazani, W. Chan, *Nano Lett.* **2006**, *6*, DOI 10.1021/nl052396o.
[28] J. Rejman, M. Nazarenus, D. J. de Aberasturi, A. H. Said, N. Feliu, W. J. Parak, *J. Colloid Interface Sci.* **2016**, *482*, 260–266.
[29] A. C. Wong, D. W. Wright, *Small* **2016**, 1–9.
[30] D. A. Lauffenburger, A. F. Horwitz, *Cell* **1996**, *84*, 359–369.
[31] S. Kurosaka, A. Kashina, *Birth Defects Res. Part C - Embryo Today Rev.* **2008**, *84*, 102–122.
[32] S. Hackenberg, A. Scherzed, M. Kessler, S. Hummel, A. Technau, K. Froelich, C. Ginzkey, C. Koehler, R. Hagen, N. Kleinsasser, *Toxicol. Lett.* **2011**, *201*, 27–33.
[33] Y. Hou, K. Cai, J. Li, X. Chen, M. Lai, Y. Hu, Z. Luo, X. Ding, D. Xu, *Int. J. Nanomedicine* **2013**, *8*, 3619–30.
[34] M. Uz, V. Bulmus, S. Alsoy Altinkaya, *Langmuir* **2016**, *32*, 5997–6009.
[35] D. Zhang, D. Liu, J. Zhang, C. Fong, M. Yang, *Mater. Sci. Eng. C* **2014**, *42*, 70–77.
[36] J. Li, J. J. Li, J. Zhang, X. Wang, N. Kawazoe, G. Chen, J. Li, X. Shi, M. Shen, D.-E.

Lee, et al., *Nanoscale* **2016**, *8*, 7992–8007.
[37] D. Zhang, D. Liu, J. Zhang, C. Fong, M. Yang, *Mater. Sci. Eng. C* **2014**, *42*, 70–77.
[38] and M. Y. Changqing Yi, Dandan Liu, Chi-Chun Fong, Jinchao Zhang, *ACS Nano* **2010**, *4*, 6439–6448.
[39] N. Artigas, C. Ureña, E. Rodríguez-Carballo, J. L. Rosa, F. Ventura, *J. Biol. Chem.* **2014**, *289*, 27105–27117.
[40] S. E. Smith, R. A. White, D. A. Grant, S. A. Grant, *J. Nanosci. Nanotechnol.* **2016**, *16*, 1160–1169.
[41] K. Baranes, M. Shevach, O. Shefi, T. Dvir, *Nano Lett.* **2016**, *16*, 2916–2920.

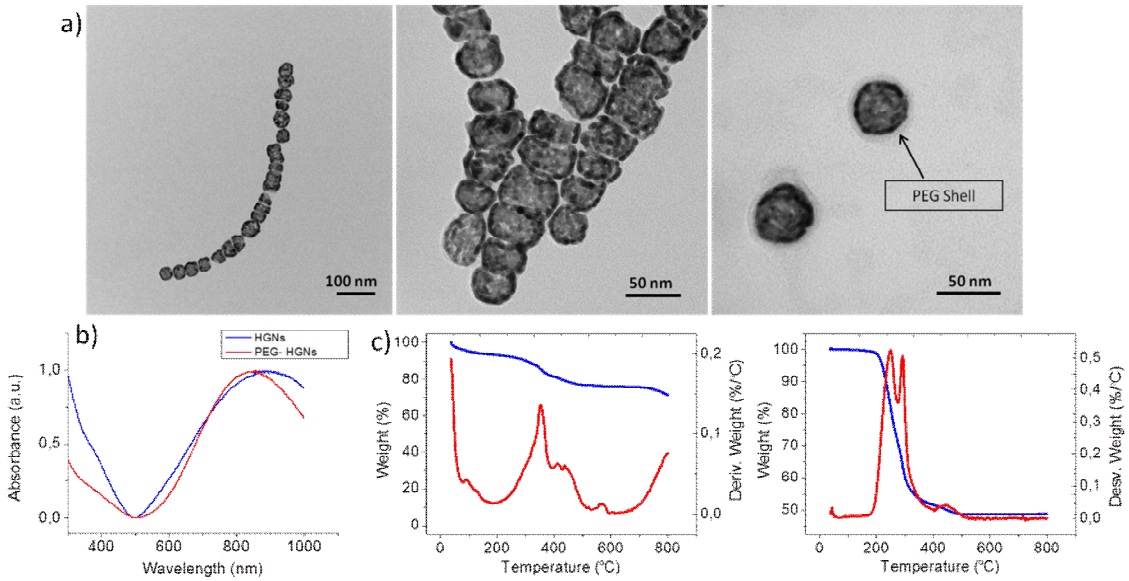

Figure 1. HGNs and PEG-HGNs characterization. a) TEM images of HGNs and PEG-HGNs. PEG functionalization is clearly visible around the nanospheres. b) UV-Vis absorption spectra for both types of nanoparticles. c) TGA results of HGNs (left) and PEG-HGNs (right).

a)

	Binding energy (eV) Atomic %				
	C 1s	O 1s	Au 4f	S 2p	N 1s
HGNs	284.9 66.40%	531.1 28.09%	83.7 5.51%		
PEG	284.9 68.18%	531.2 30.19%		162.3 1.36%	398 0.27%
PEG-HGNs	284.9 75.91%	531.2 22.22%	83.5 0.42%	162.4 0.48%	399 0.97%

b)

	$S2p_{3/2}$ Binding energy (eV) Atomic %	
	S-H	S-Au
PEG	163.7 100%	
PEG-HGNs		162.4 100%

	Au 4f 7/2 Binding energy (eV) Atomic %	
	Au^0	Au-S
PEG-HGNs	83.6 **12%**	85.0 **88%**

c)

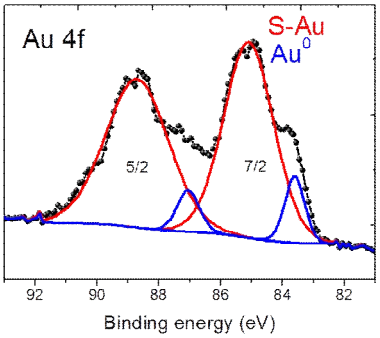

Figure 2. XPS of HGNs and PEG-HGNs. a) Elemental composition of HGNs and PEG-HGNs. b) Binding energies and peak assignation for S2p $_{3/2}$ and Au 4f $_{7/2}$ core levels PEG-HGNs; c) Au 4f core level spectrum. The blue line indicates the binding energies of the elemental gold and the red line indicates the binding energies of the gold bound to sulfur.

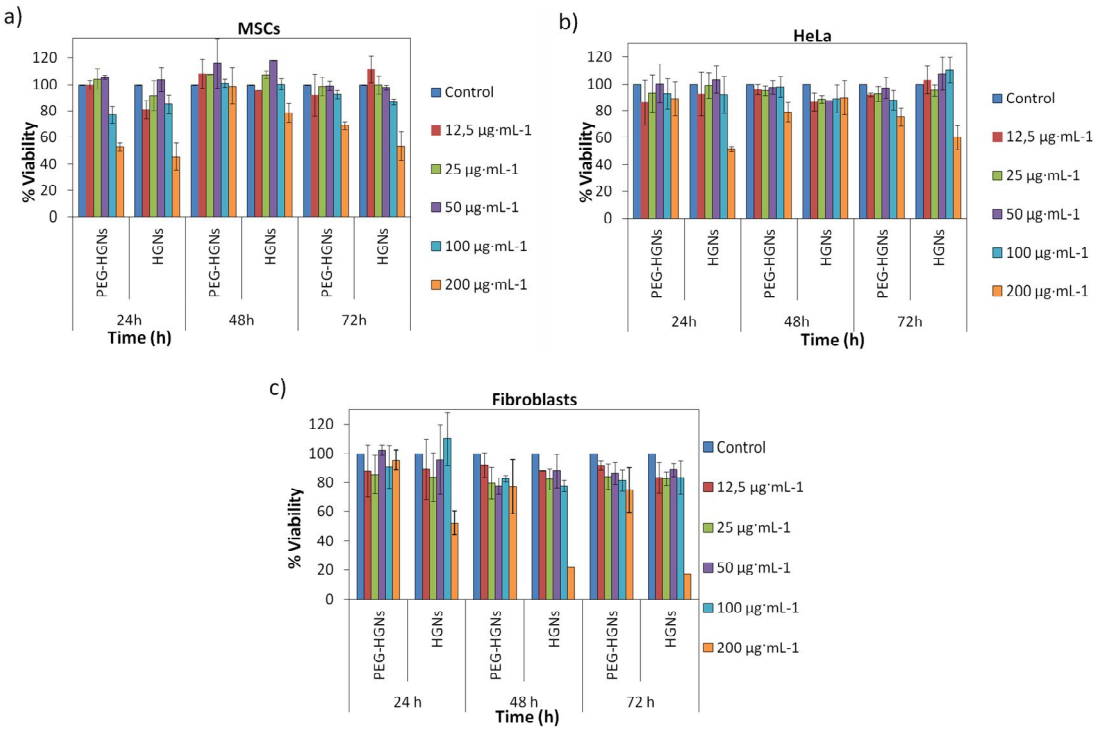

Figure 3. **Cytotoxicity analysis.** AlamarBlue® results for a) MSCs; b) HeLa cells; and c) human dermal fibroblast after incubation with HGNs or PEG-HGNs during different times. (n=3)

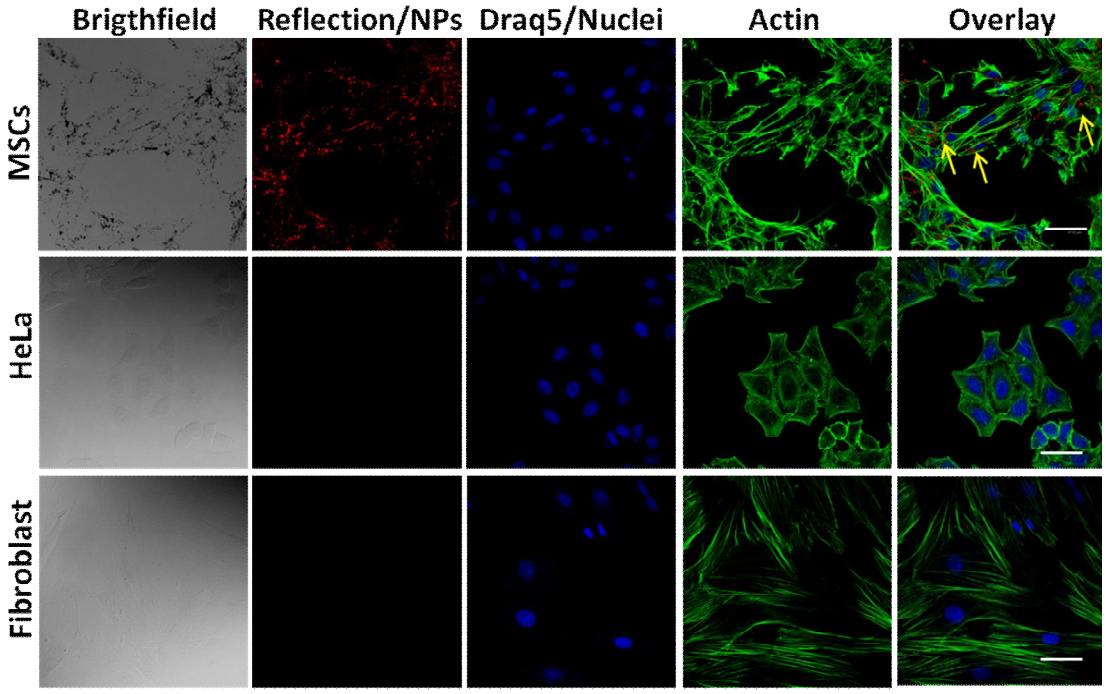

Figure 4. HGNs and PEG-HGNs internalization evaluation by confocal microscopy. In order to visualize the cytoplasm of the cells, the actin was labeled with phalloidin-488, whereas the nuclei were stained with Draq5. PEG-HGNs were directly visualized by reflection. In all cases, a Z-stack was done to confirm the internalization of the particles. PEG-HGNs agglomerates were only observed inside MSC. The yellow arrows indicate the location of nanoparticles within the cells.

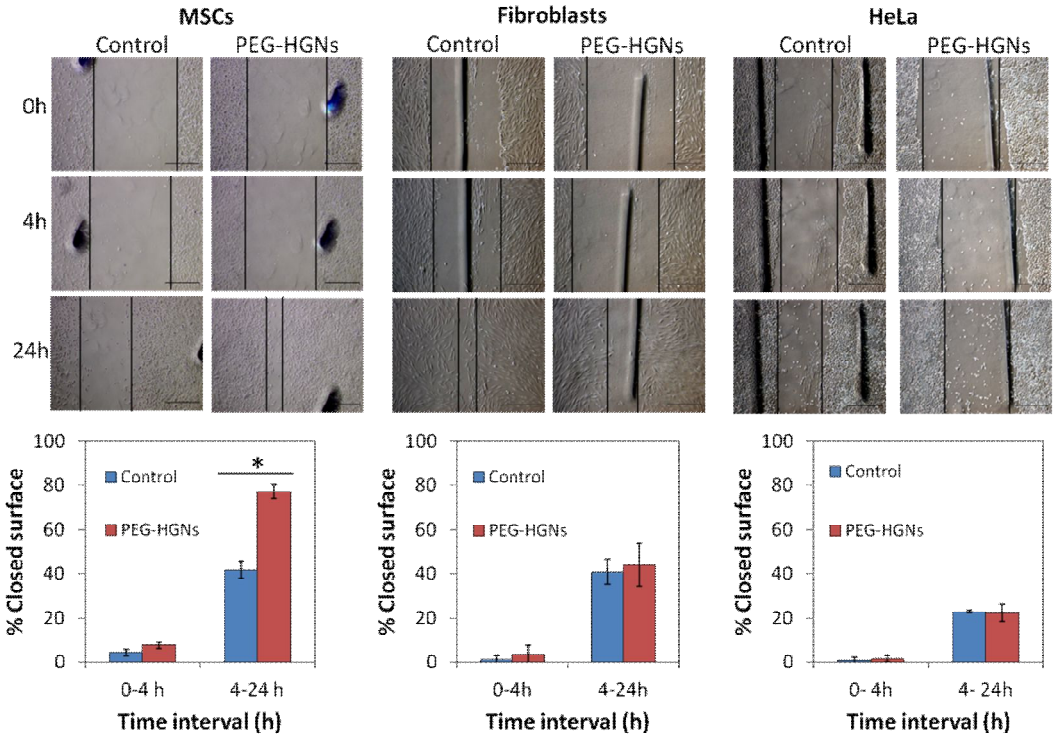

Figure 5. Migration evaluation. a) Scratch assay in MSCs, HeLa cells and fibroblasts incubated without (control) or with PEG-HGNs (50 µg mL^{-1}) evaluated by inverted optical microscope. (Scale bar = 500 µm). b) Quantitative analysis of relative cell migration for 0, 4 and 24 h. The differences between the closed surface at different intervals of time are shown. Significant differences ($p<0.05$) between the percentage of closed surface among the control and MSCs incubated with PEG-HGNs were observed.

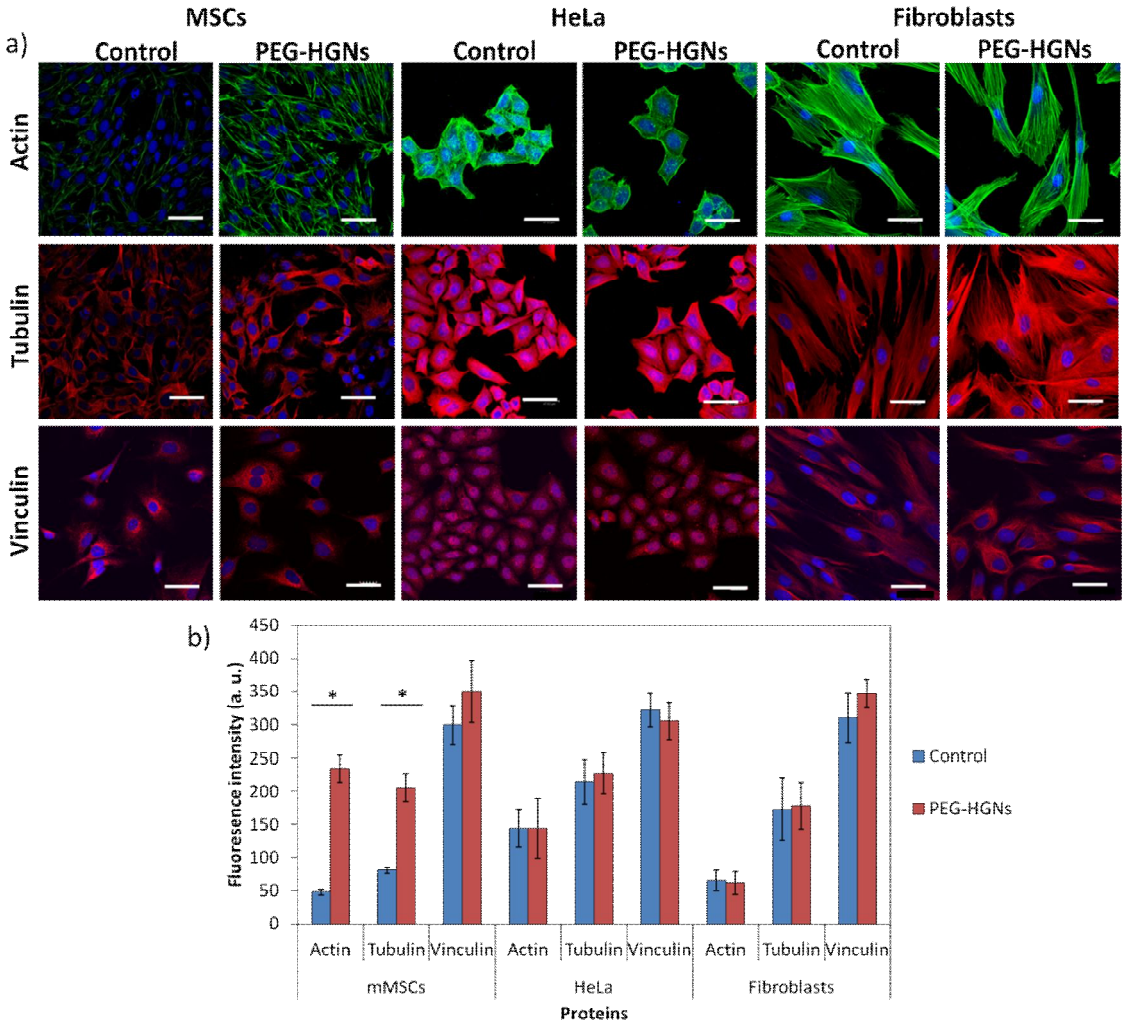

Figure 6. Actin and tubulin expression evaluation. a) Immunoassay study for proteins by confocal microscopy. Actin was labeled with phalloidine-488 and tubulin and vinculin were marked with and specific antibody. (Scale bar = 47.7 µm). b) Relative fluoresce intensity analysis of actin, tubulin and vinculin in the three cellular types. Significant differences between the control and the treated cells were observed for MSCs ($p<0.05$).

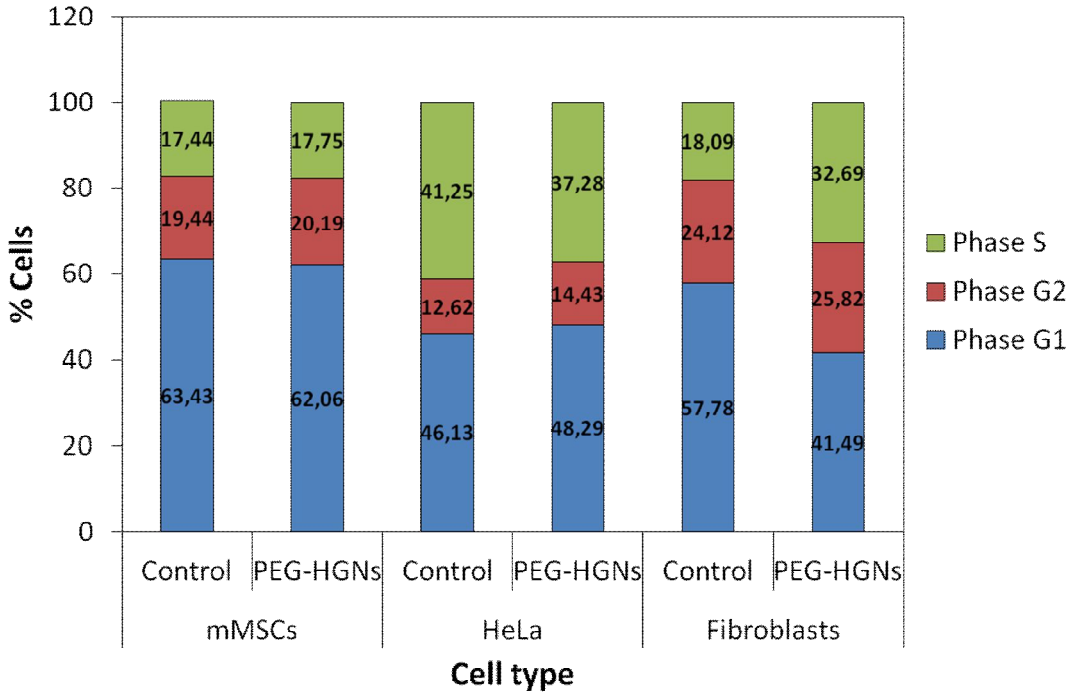

Figure 7. Cell cycle analysis. The three cellular types were incubated with PEG-HGNs at a concentration of 50 $\mu g \cdot mL^{-1}$ during 24 h.

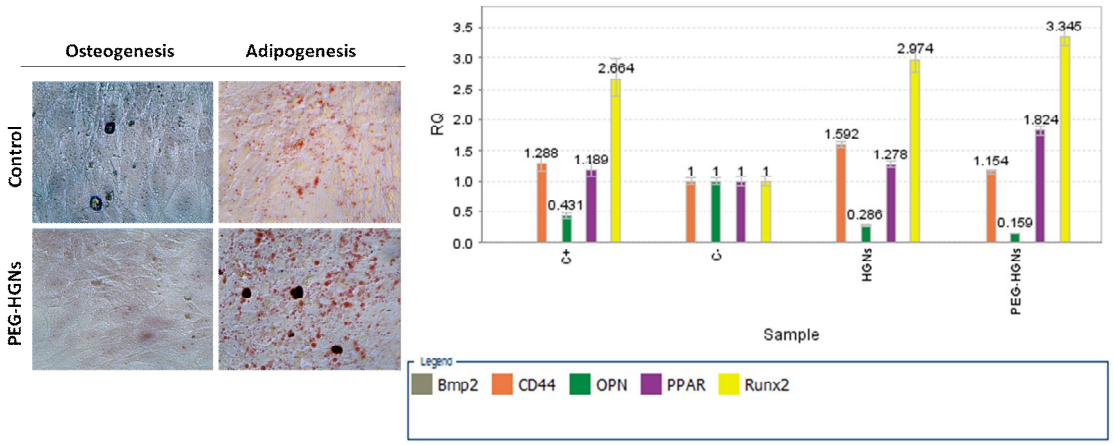

Figure 8. Differentiation evaluation. The images represent the typical staining for osteogenic (Alizarin Red) and adipogenic (Oil Red) differentiation. The graph shows gene expression of osteogenic markers genes.

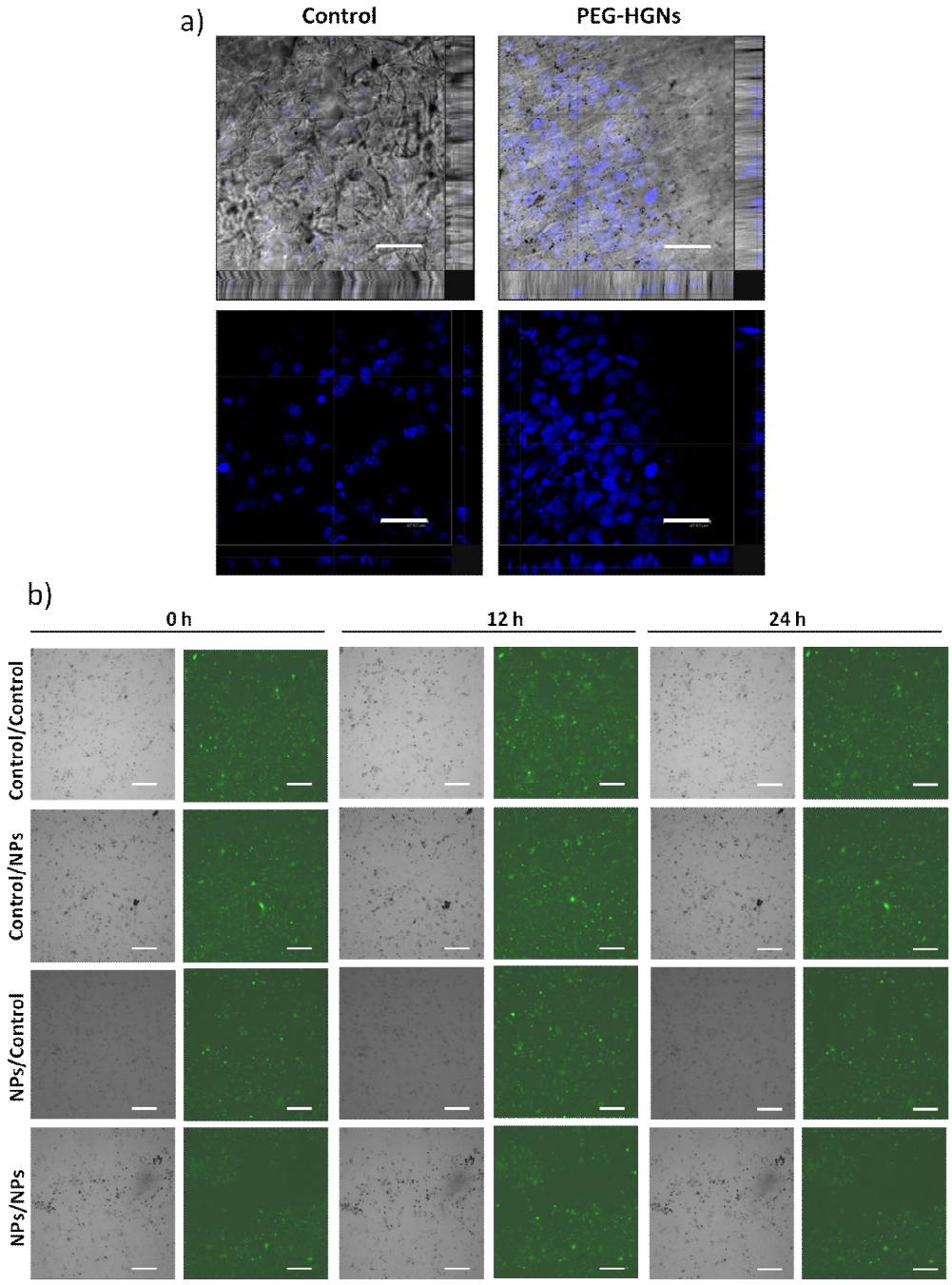

Figure 9. Scaffold colonization. a) PCL membranes colonization by control cells or cells with internalized PEG-HGNs 24 h after seeding the cells. Scale bar: 47,6 µm. b) Fibrin scaffold colonization by MSCs incubated with or without PEG-HGNs. In the first row the photos show control cells seeded onto control scaffolds. The second row represents control scaffold colonization by cells incubated with PEG-HGNs. The third row shows the colonization of a fibrin gel with PEG-HGNs by control cells. In the last row both the cells and the gel contained PEG-HGNs. Scale bar: 254 µm.